▌**Metal Oxide Nanoparticles** │*Hot Paper*│

Designing Metallic MoO$_2$ Nanostructures on Rigid Substrates for Electrochemical Water Activation

Vivek Ramakrishnan, C. Alex, Aruna N. Nair, and Neena S. John*[a]

Abstract: In situ growth of metallic MoO$_2$ films on fluorine-doped tin oxide (FTO) and MoO$_2$ powder in solution was achieved simultaneously by a simple hydrothermal process employing citric acid as the surfactant. The growth mechanism of MoO$_2$ nanostructures (NSs) at the heterogeneous interface and in homogeneous medium proceeds in a different manner in which seeds grow in a preferred orientation on FTO, whereas they propagate in all directions in solution. The high lattice matching of FTO and MoO$_2$ favours the film growth which could not be obtained on other conventional substrates. The disc morphology of MoO$_2$ nanostructures was changed to other diverse morphology by varying the synthesis conditions, particularly by the addition of nitric acid. A competitive effect of nitric acid and citric acid on the structure direction produced various shapes. The electrochemical water activation studies show that hydrogen-annealed MoO$_2$ is an excellent hydrogen evolution reaction (HER) catalyst with good stability. H-MoO$_2$ film/FTO displays a low onset overpotential of 72 mV with a Tafel slope of 84.1 mV dec^{-1}, whereas the powder form exhibits an onset overpotential of 46 mV with a Tafel slope of 71.6 mV dec^{-1}. The large active surface area, exposure of fringe facets of (110) and the lesser electrochemical charge-transfer resistance offered by the hydrogen-annealed MoO$_2$ NSs play a major role in the enhanced HER activity.

Introduction

There is a growing demand for new pathways to produce a clean, renewable and sustainable energy source as an alternative to fossil fuels that are quickly getting depleted and that are detrimental to the environment. From this perspective, the use of hydrogen could be the best possible solution if hydrogen could be produced, stored and utilized in a cost-effective way. Electrocatalytic water splitting is one of the most powerful routes to produce hydrogen.[1] Even though platinum is still the benchmark catalyst for hydrogen evolution reaction (HER) because of an almost zero overpotential, high cost and paucity drive the search for alternative HER catalysts.[2]

Transition-metal oxide-based systems with desirable structure, morphology, orientation, dimensionality and bandgap tunability have attained significant interest in recent years because of potential applications ranging from microscopic to macroscopic real-world devices arising from their diverse catalytic, magnetic, optical, semiconducting and other superior properties.[3] Molybdenum dioxide-based systems are shown to have a wide variety of applications as such or when coupled with metal chalcogenides.[4] MoO$_2$ is a promising functional material reported to have metallic as well as semiconducting properties depending on the preparation method and subsequent treatment.[5] MoO$_2$-emanated systems have found diverse applications in catalysis,[6] light-emitting diodes,[7] sensors,[8] batteries,[9] fuel cells, photo- and electrocatalysts,[10,11] and photochromic and electrochromic[12] systems owing to its structure-, size- and shape-dependent properties. MoO$_2$-based systems show high metallic electrical conductivity (8.8 × 10^5 Ω cm^{-1} at 300 K in bulk samples),[5b] melting point, density (6.5 g cm^{-3}),[13] and high chemical stability.[14] Many approaches have been reported for the preparation of MoO$_2$ micro-nano structures, namely, hydrothermal,[14] chemical vapour deposition,[15] electron beam-[16] and laser beam-induced deposition,[17] microwave irradiation[18] and so on. MoO$_2$ is reported to have three polymorphic forms: thermodynamically stable monoclinic ($P2_1$), tetragonal ($P4_2/mnm$) and hexagonal ($P6_3/mmc$).[9] Monoclinic MoO$_2$ has lattice parameters $a = 5.6068$ Å, $b = 4.8595$ Å and $c = 5.5373$ Å. In this structure, O atoms are closely packed into octahedrons, and Mo atoms occupy half the space of the octahedral void. The reverse edge-sharing MoO$_6$ octahedra connect with each other to form a deformed rutile structure (Figure 1a). When compared with MoO$_3$, MoO$_2$ contains two kinds of Mo—Mo metallic bonds with different bond lengths (Mo—Mo bond distances of 0.25 and 0.31 nm), which renders good electrical conductivity—the conductivity is almost 3 times higher than MoO$_3$.[5a,c]

Recent works indicate that MoO$_2$ could be a potential candidate as an electrocatalyst for HER. Jin and Shen reported HER electrocatalytic performance of nanoflower-like MoO$_2$ in alkaline electrolytes.[14] Hierarchically structured 1D MoO$_2$ also showed superior electrocatalytic activity and long-term stabili-

[a] Dr. V. Ramakrishnan, C. Alex, A. N. Nair, Dr. N. S. John
Centre for Nano and Soft Matter Sciences (CeNS)
Jalahalli, Bengaluru 560013 (India)
E-mail: jsneena@cens.res.in
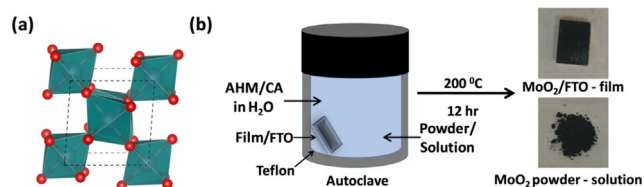
Figure 1. Schematic diagram of (a) the unit cell of monoclinic MoO_2 and (b) hydrothermal synthesis.

Figure 2. (a) XRD pattern, (b) Raman spectra, and FESEM images and zoom-in views (inset) of hydrothermally grown MoO_2 NSs (c) on FTO and (d) in solution prepared by using 0.02 M AHM and 0.1 M CA at 200 °C for 12 h.

ty for HER, as reported by Li et al.[19] However, the achieved HER electrocatalysts based on MoO_2 are still less satisfactory, and hence, improved synthesis strategies to enhance their HER properties are worth exploring.

The controlled synthesis of metallic and semiconducting nanomaterials as thin films on substrates holds substantial interest for many applications. In a recent study, Symes and co-workers reported the hydrothermal assisted growth of Co-doped MoS_2 on fluorine-doped tin oxide (FTO) for HER.[20] Even though there are numerous reports on the synthesis and electrocatalytic activity of nanostructured MoO_2 in the powder form, to the best of our knowledge, the current study is the first attempt at growing uniform metallic MoO_2 film on a rigid conducting substrate. The systematic study of several factors affecting the structure, composition, shape and morphology of MoO_2 nanostructures (NSs) is presented along with the HER activity.

Results and Discussion

Microstructure of MoO_2 film

The synthesis scheme for obtaining MoO_2 film on FTO and MoO_2 powder from solution by employing 0.02 M ammonium heptamolybdate tetrahydrate (AHM) and 0.1 M citric acid (CA) at 200 °C for 12 hours is shown in Figure 1b. The X-ray diffraction (XRD) pattern of the black film and the powder are given in Figure 2a. The major peaks correspond to (110), (020), (200), (220), (211), (310) and (202) of monoclinic MoO_2 (JCPDS #65-5787) in the case of both the film and powder. The peaks due to FTO are marked with an asterisk (*). From XRD, it can be deduced that the formed MoO_2 is devoid of its polymorphs or other forms of molybdenum trioxides.

In the case of FTO, a few peaks due to the substrate are merged with MoO_2 peaks. For clarification, zoom-in views of the plot are shown in Figure S1. In addition, the MoO_2 film on FTO has a preferred orientation with the (200) plane, whereas the powder form consists of NSs with the (110) plane showing high intensity.

Figure 2b shows the Raman spectra of the MoO_2 NSs on FTO and the powder, which matches very well with the reported data.[5a,14,21] The fingerprint bands due to phonon vibration modes of MoO_2 are observed at 486, 346, 284 and 198 cm^{-1} for both film and powder. Vibration modes at 991 and 818 cm^{-1} are attributed to stretching of ν(Mo-O-Mo) and ν(Mo=O), respectively.[22]
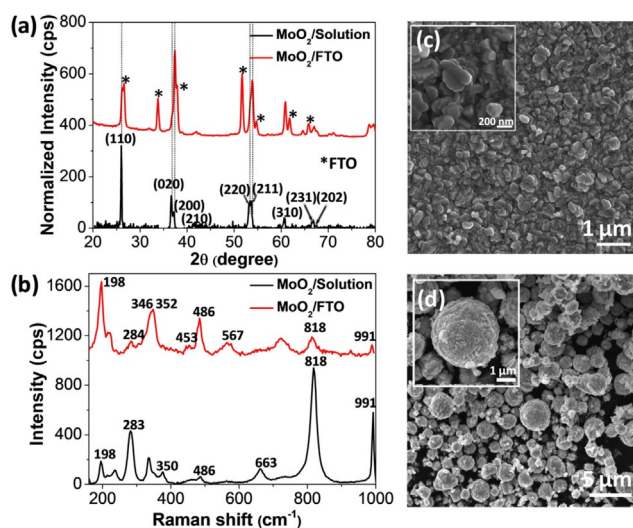
The morphology of the as-synthesized MoO_2 film on FTO and the powder were examined by field emission scanning electron microscopy (FESEM). The top view of the MoO_2 film on FTO is shown in Figure 2c. The film consists of densely grown disc-shaped NSs on FTO. The average area of the particles was calculated to be 0.03 μm^2. The black powder retrieved from the solution under the same reaction conditions contained micron-sized spheres consisting of crystallites growing in all directions (Figure 2d). Energy dispersive spectroscopy (EDS) analysis shows that the sample consists of Mo and O (Figure S2). The NSs obtained on FTO clearly depict heterogeneous nucleation at the FTO/solution interface, whereas that obtained from solution indicates homogeneous nucleation in all directions.

MoO_2 NSs formed on FTO were also examined by transmission electron microscopy (TEM). The low-resolution TEM image shown in Figure 3a confirms the disc-shaped morphology. The selected area electron diffraction (SAED) pattern of MoO_2 NSs (Figure 3b) shows diffraction due to (110) and (200) planes.

The chemical composition of MoO_2 NSs was investigated by X-ray photoelectron spectroscopy (XPS). As shown in Figure S3, there are five peaks in the survey spectra of the MoO_2, which can be indexed to Mo 3d (232.1 eV), C 1s (283.8 eV), Mo 3p (396.4 and 414.4 eV) and O 1s (529.2 eV). Deconvoluted Mo 3d spectra (Figure 3c) show distinct peaks at 229.5 and 232.7 eV that can be assigned to Mo 3d$_{5/2}$ and Mo 3d$_{3/2}$ of the Mo^{4+} state, respectively.[5a,14] The low-intensity peaks corresponding to the binding energies 231.2 and 234.7 eV are consistent with Mo 3d$_{5/2}$ and Mo 3d$_{3/2}$ of the Mo^{5+} state arising from the surface hydrated species of MoO_{3-x}.[23] The XPS spectra of O 1s is given in Figure 3d, and it indicates the presence of three types of oxygen species corresponding to molybdenum oxides, surface-adsorbed oxygen from the surfactant and surface -OH
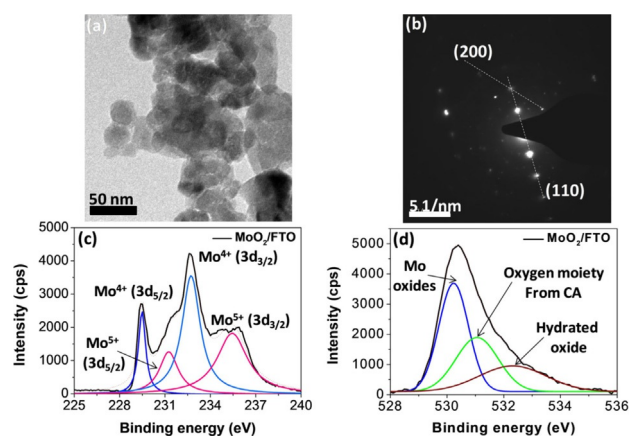
Figure 3. (a) Low-resolution TEM image, (b) SAED pattern and XPS spectra of (c) Mo 3d and (d) O 1s from MoO_2/FTO prepared by using 0.02 M AHM and 0.1 M CA at 200 °C for 12 h.

groups with binding energy values of 530.1, 531 and 532.3 eV, respectively.[14,23a]

Thermogravimetric analysis (TGA) and differential thermal analysis (DTA) measurements of MoO_2 powder were carried out under nitrogen and air. In air (Figure S4a), an exothermic peak appeared at ≈ 400 °C in DTA, accompanied by an increase in weight percentage in TGA. This can be associated with the conversion of MoO_2 to MoO_3 as a result of oxidation by correlating the molecular weight of MoO_2 and MoO_3 to the initial and final weight percentage.[24] XRD and FESEM reveal that monoclinic MoO_2 converted to α-MoO_3 during annealing under air at 400 °C, in agreement with the results of the TGA/DTA (Figure S5). The above phase transition is further substantiated by the absence of an exothermic peak during heating under nitrogen, and a gradual decrease in the weight percentage is seen, indicating the retention of the monoclinic phase of MoO_2 (Figure S4b).

Effect of synthesis parameters on MoO_2 film/FTO

The effects of various synthesis parameters (such as reaction temperature and time, surfactant concentration, type of Mo precursor, surfactant, substrate and also addition of nitric acid) on the structure, chemical composition and morphology were systematically studied, and the results are summarized in Tables S1–S5 and Table 1.

Effect of temperature

Monoclinic MoO_2 with disc-shaped morphology was obtained at the standard reaction temperature of 200 °C. At lower temperature, 120 °C, a reaction did not happen. At 150 °C, monoclinic MoO_2 with almond-like morphology was obtained (Figure S6 and Table S1).

Effect of reaction time

After the saturation time of 12 hours, further increase in time did not have much influence on the shape and crystal structure of the individual NSs. XRD and Raman spectra show that the MoO_2 phase was still preserved (Figure S7a,b). However, the crystallites constituting the films seem to have grown further with a change in the orientation with longer reaction times. Accordingly, we see a change in the intensity maximum from the (200) to (110) peak in the XRD pattern. The size of MoO_2 NSs seems to have increased for the 48 hour reaction and is evident from the FESEM images (Figure S7c,d and Table S2). The calculated area of the particles for the 30 hour reaction and the 48 hour reaction are 0.03 and 0.1 μm^2, respectively.

Effect of CA concentration

CA is found to have a crucial role in MoO_2 formation in the reduction of Mo^{VI} to Mo^{IV}, as well as in defining morphology and size, as evident from FESEM analysis. The reaction did not happen in the absence of CA. When the concentration of CA was varied from 0.1 M to 0.2 M, the morphology changed from disc to dome-like (Figure S8a and Table S3). Moreover, the MoO_2 NSs were found highly oriented in the (110) direction as the concentration of CA was doubled (Figure S8c). When the concentration was further increased to 0.4 M, the morphology changed to smaller particles forming a thin film (Figure S8b). In the XRD pattern, the high intensity of the FTO peaks masks the peaks due to polycrystalline MoO_2 nanoparticles (Figure S8c). Raman spectroscopic analysis further confirmed the presence of monoclinic MoO_2 (Figure S8d). When the CA concentration was increased, it acted more like a capping agent, causing size reduction and therefore smaller particles. Figure 2c and Figure S8 clearly show that the particle size is decreasing with the increase in the concentration of the surfactant. The adsorption of the surfactant molecules on the nanoparticles hinder further growth.[25]

No.	AHM [M]	HNO$_3$ [mL]	CA [M]	Water [mL]	Temp. [°C]	Time [h]	Result	Chemical & physical composition
1	0.02	1 (1 M)	0.1	40	200	12	black film	MoO_2/monoclinic/fiber-covered discs
2	0.02	3 (1 M)	0.1	40	200	12	black film	MoO_2/monoclinic & hexagonal/distorted rectangular rods
3	0.02	6 (1 M)	0.1	40	200	12	black film	MoO_2/monoclinic/pseudo-hexagonal rods
4	0.02	1 (1 M)	0.1	40	150	12	black film	MoO_2/monoclinic & hexagonal/particulate film
5	0.02	1 (1 M)	0.1	40	120	12	white film	MoO_3/hexagonal/hexagonal rods
6	0.02	5 (concd)	0.1	40	200	12	white film	MoO_3/alpha/rods

Table 1. Effect of variation of HNO$_3$ concentration.

Effect of Mo precursor

The growth of MoO_2 NSs was carried out by substituting the Mo precursor AHM with $MoCl_5$ and bis(acetylacetonato)dioxomolybdenum(VI) (MoAcac). Interestingly, the NSs formed in these cases also appeared in the form of a uniform black film characterized as monoclinic MoO_2 (Figure S9a,b). However, the morphology of MoO_2 is different in each case: disc-shaped morphology from AHM, rod-like structure from $MoCl_5$ and aggregated particles from MoAcac (Figure S9c,d and Table S4).

Effect of surfactant

To understand the effect of the surfactant type, CA was replaced by ascorbic acid (AA) in the standard reaction. Even though the morphology was entirely different from that of CA-induced MoO_2 NSs (Figure S10a), the monoclinic phase and chemical composition were conserved as shown by XRD and Raman spectroscopic analysis (Figure S10b,c and Table S5). The film obtained in this case consisted of aggregated nanoparticles.

Effect of substrate

Another important factor is the substrate effect. Experiments were carried out by placing different substrates (like glass, Si, SiO_2 and FTO) in the same reaction pot. Interestingly, there was hardly any MoO_2 growth on the other substrates except for FTO. The obvious reason for MoO_2 growth observed on FTO is because of the high lattice matching.[26] The major planes of FTO (110), (200) and (211) and that of MoO_2 have closely matching d spacing values (JCPDS #01-077-0452).

Effect of HNO₃

The addition of HNO_3 was found to have a crucial role on the morphology as well as on the crystal structure. The amount of HNO_3 was varied as 1, 3 and 6 mL (0.021, 0.023 and 0.025 M) using a stock solution of 1 M HNO_3 (Table 1). Even this slight change in concentration of 4 mM caused a drastic change in the morphology ranging from fibre-covered disc-shaped particles to distorted rectangular rods to pseudo-hexagonal rods for 1, 3 and 6 mL samples, respectively (Figure 4a–c). The size of the MoO_2 crystallites obtained also seems to increase from nanoparticles to micron-sized cylinders with the increase in the amount of HNO_3. The crystal structure remained unchanged as monoclinic for the 1 and 6 mL samples, whereas the 3 mL sample was found to be a mixture of monoclinic and hexagonal crystallites as evident from the XRD analysis (Figure 4e). The (100) and (102) planes of hexagonal MoO_2 are the major peaks in the 3 mL samples (JCPDS #500739) in addition to the (110) plane, which corresponds to monoclinic MoO_2. Raman spectra further confirmed the formation of MoO_2 in all cases of 1 M HNO_3 addition (Figure 4f). With the addition of 1, 3 and 6 mL of 1 M HNO_3, the pH of the system was found to vary as 2, 1.75 and 1.45, respectively. However, when the reaction was performed using concentrated HNO_3 under standard condi-
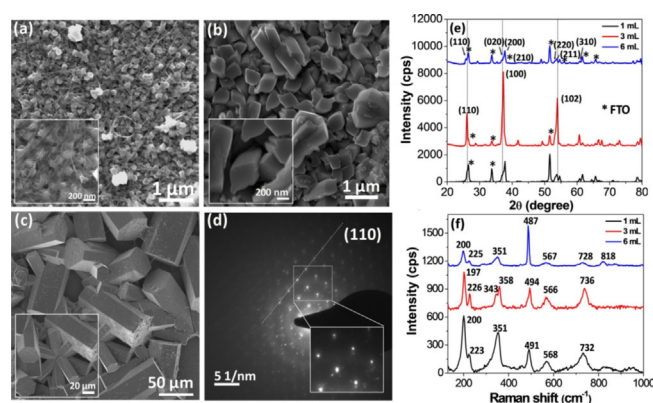

Figure 4. FESEM images and zoom-in views (inset) of hydrothermally grown MoO_2/FTO NSs prepared by using 0.02 M AHM and 0.1 M CA at 200 °C for 12 h and by varying the 1 M HNO_3 amount: (a) 1 mL, (b) 3 mL and (c) 6 mL. (d) SAED pattern and zoom-in view (inset) of pseudo-hexagonal-shaped MoO_2/FTO NSs (1 M HNO_3, 6 mL). (e) XRD pattern and (f) Raman spectra of MoO_2/FTO NSs (1 M HNO_3, 1, 3 and 6 mL).

tions with AHM and CA at 200 °C, the thermodynamically stable phase of α-MoO_3 nanorods was obtained (Figure S11 and Table 1). This is expected because the large amount of H^+ ions favours the formation of MoO_3, overshadowing the effect of the reducing surfactant CA.[27]

Pseudo-hexagonal morphology formed by monoclinic MoO_2 from 6 mL of 1 M HNO_3 is of particular interest, and we further looked at the crystal structure using TEM. The SAED pattern shows the prominent peak of the monoclinic phase (110) consistent with the XRD analysis (Figure 4d). However, the presence of vivid split spots in the SAED pattern indicates the presence of twin domains arising from separate reflections of adjacent domains (inset of Figure 4d). The pseudo-hexagonal morphology could be arising from a twinning effect.[28] These MoO_2 pseudo-hexagons could be formed as a result of six-fold twinning, with six triangular domains touching at the centre of the crystal, which also suggests that twinning might have already occurred at the initial stages of nucleation.[29] We also observed a branched growth of fused pseudo-hexagons, further suggesting the presence of twinning fault lines (inset of Figure 4c).

We also varied the reaction temperature in the above experiments with 1 mL of 1 M HNO_3. When the temperature was lowered to 150 °C, MoO_2 was still obtained (Figure S12a,c,d), and interestingly, these samples were found to be a mixture of both hexagonal and monoclinic MoO_2. Further lowering of the temperature (120 °C) was found to favour metastable hexagonal MoO_3 (h-MoO_3) as shown in Figure S12b and confirmed by XRD (Figure S12c) and Raman spectroscopy (Figure S12d).

Mechanism of MoO₂ NSs formation

To understand the growth mechanism, the time-dependent growth of MoO_2 NSs was monitored in solution and on FTO. The standard reaction using 0.02 M AHM with 0.1 M CA at 200 °C was performed in a sealed vessel and quenched at particular time intervals (45, 90, 120 and 180 minutes), and the re-

action was freshly performed in each case. The resulting products were characterized by FESEM, XRD, and Raman and infrared (IR) spectroscopy (Figure 5 and Figure 6). At 45 minutes, a pale-bluish precipitate was obtained in solution as well as on FTO. XRD and Raman spectra did not give any signatures corresponding to intermediate oxides of molybdenum (Figure 5b–e). Various bluish-colored intermediates have been reported for Mo-based systems when reduced under acidic conditions (pH < 2)[30] and do not represent a definite oxidation state or a unique compound.[30] The morphology of the film on FTO and the pale-bluish precipitate formed in solution showed a very smooth texture with no features (Figure 5a(i,vi)). IR spectra of the precipitate obtained in solution indicates the presence of citric acid, and a redshift in the C=O stretching frequency indicates its coordination with Mo ions (Figure 6a,b).[31] Hence, we
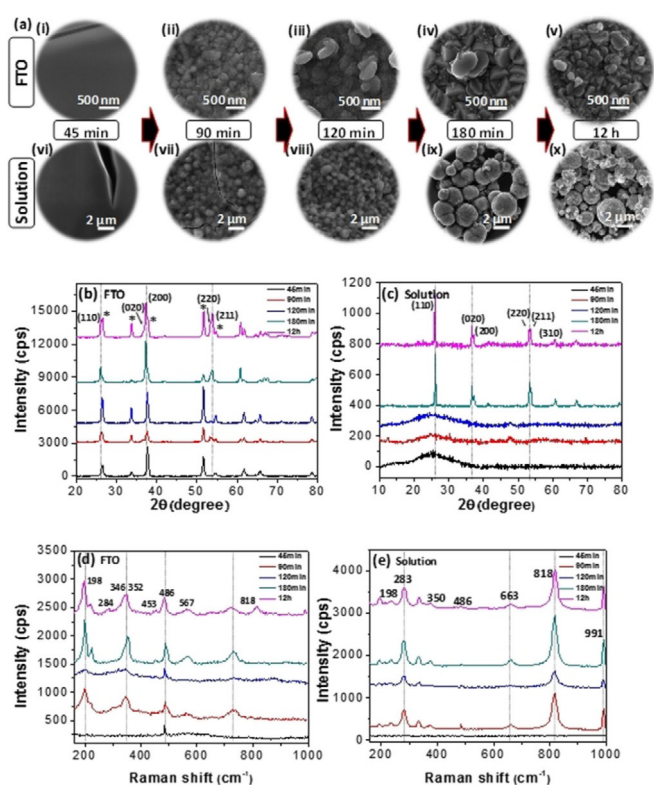
propose that at 45 minutes, AHM coordinated with CA molecules were possibly formed. At 90 minutes, black film and powder were obtained, and the Raman spectra clearly indicate the formation of MoO_2 particles. FESEM images (Figure 5a) also show the presence of nanoparticles in both the powder and film. At more than 90 minutes of reaction time (i.e., at 120 and 180 min), the particles increased in size, and crystallinity improved with the appearance of distinct peaks due to monoclinic MoO_2 in the XRD patterns. Time-dependent IR spectra (Figure 6a) shows that the amount of CA present in the product decreases with reaction time, indicating that CA molecules are used up in a reduction reaction forming MoO_2 NSs.

A change in the morphology of MoO_2 particles constituting the film and powder is seen at 90 minutes of reaction, indicating that growth proceeds differently at a heterogeneous interface and in homogeneous environment. In solution, sheets of MoO_2 oriented to form flower-like nanostructures are seen at 90 minutes (Figure S13), whereas on FTO, spherical nucleates on sheet structures are observed. Further reaction in solution for 120 and 180 minutes results in the growth of sheets in all directions due to homogeneous nucleation and flower-like nanostructures transform to microspheres that consist of MoO_2 nano-discs. On FTO, the spherical NSs on sheets grow further to form well-developed discs with preferred (200) orientation for 120 and 180 minutes duration of reaction (Figure 5a,b). Time-dependent studies also indicated faster reaction kinetics in the case of FTO, in which MoO_2 crystalline peaks started to originate even at 120 minutes but in-solution peaks originated only at 180 minutes, which evidently gives an insight into the crucial role of FTO (Figure 5b,c). However, Raman spectroscopic analysis shows that even the spherical agglomerates formed in solution at 90 minutes correspond to MoO_2 NSs (Figure 5d,e).

We also tried to understand the role of CA in the formation of MoO_2 NSs. CA plays a significant role as a reducing agent for reducing Mo ions that exist in the higher oxidation state in the precursors employed for the reaction. CA can also act as a surfactant in stabilizing the NSs obtained. The time-dependent FTIR spectra shown in Figure 6 provide evidence for the coordinating nature of CA to MoO_2. Strong absorption peaks are observed at 3500 and 1718 cm^{-1}, attributed to the stretching of the hydroxyl group and carboxyl group, respectively (Figure 6a). The intense band at 1740 cm^{-1} observed for the free CA molecule, as a result of the carbonyl stretching vibration (ν(C=O)), is shifted to ≈1718 cm^{-1} as the reaction proceeds (Figure 6b). The shift towards a lower wavenumber arises as a result of the weakened C=O bond due to its interaction with the MoO_2. It has been reported that CA molecules may coordinate to metal oxide NSs by adsorption through at least one carboxylate group.[32]

To further account for the existence of CA molecules interacting with the crystal lattice, we analyzed the TGA results of MoO_2 NSs under nitrogen, which gave three distinct steps during the thermal decomposition process (Figure S14). The first step (up to 150 °C) is attributed to the removal of water molecules, whereas the second (150–300 °C) and third steps (300–500 °C) are ascribed to the loss of surface-[31] and lattice-adsorbed organic moiety (CA), respectively. These observations

Figure 5. Time-dependent growth of MoO_2 NSs on FTO and in solution monitored by (a) FESEM, (b,c) XRD and (d,e) Raman spectra.
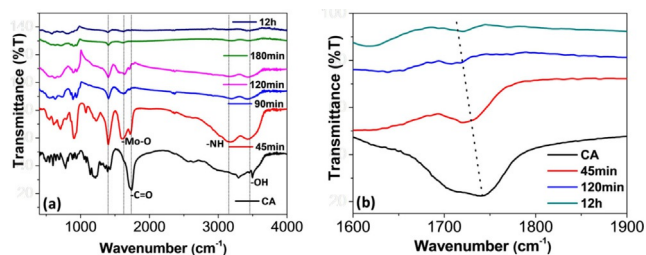

Figure 6. (a) Time-dependent growth of MoO_2 NSs in solution monitored by IR spectroscopy. (b) Expanded view showing the shift of C=O stretching with time due to coordination with the metal (Mo) ion.

match those of previous reports.[33] To show that the MoO$_2$ phase is retained during the thermal decomposition, a set of annealing experiments (100, 200, 300 and 400 °C) were conducted under nitrogen. From the FESEM, XRD and Raman spectroscopic analyses given in Figures S15 and S16, we can clearly assimilate that the morphology, chemical composition and monoclinic phase remained intact until 300 °C. Annealing at 400 °C under inert conditions transformed the disc-shaped morphology to rectangular morphology (Figure S15d), albeit the chemical composition and monoclinic phase remained unaltered. IR spectra of 400 °C-annealed samples showed completely diminished peaks due to CA (Figure S17a), indicating the removal of citric acid at this stage. ^{13}C NMR spectroscopic analysis of MoO$_2$ NSs before and after annealing under inert atmosphere shows the disappearance of CA molecules at 400 °C annealing (Figure S17b). The removal of CA molecules could be causing the change of morphology from disc to basic monoclinic rectangular shape. Such a type of structure direction and stabilization of nanoparticles by CA molecules have been reported for ZnO nanorods in which the structure collapses to polygon granules upon annealing.[34] In work reported by Wang et al., CA molecules play the crucial role in tuning the morphology of NiO nanofibers by calcination at different temperatures.[35] These reports complement our results in which CA molecules are coordinated to MoO$_2$ and are removed only above 300 °C. In the literature, there are numerous reports for CA-assisted inorganic syntheses of various nanostructured materials.[36]

Another important aspect of MoO$_2$ NSs formation is the key role of HNO$_3$. The lower-temperature (120 °C) reaction was dominated by HNO$_3$, and the higher-temperature reaction was dominated by CA. At lower temperature, there was no reaction with CA alone, whereas in the presence of HNO$_3$, h-MoO$_3$ was formed. Monoclinic MoO$_2$ was favoured at higher temperatures with CA alone as well as with CA and HNO$_3$. From these results, we can elucidate that CA is active only above 150 °C, and the activity of 1 M HNO$_3$ is prominent below 150 °C.

If concentrated HNO$_3$ is used as such, then irrespective of temperature and CA concentration, the former has the crucial role in leading to the formation of α-MoO$_3$. Under the standard reaction conditions, when a small amount of HNO$_3$ is added, there is competition between HNO$_3$ and CA molecules.[27b] In the presence of HNO$_3$, H$^+$ ions and NO$_3^-$ ions can also interact with MoO$_6$ growth units, interfering with CA coordination and causing morphological changes and the formation of larger crystallites (Figure 4a–c).

Metallic properties of MoO$_2$ film

To measure the conductivity of the as-prepared MoO$_2$ films, they were etched from the FTO substrate using HF and transferred onto a glass substrate. Current-voltage (I-V) characteristics were determined by a two-probe method. Figure 7 shows that I versus V is symmetrical and linear, in agreement with Ohm's law and indicating the metallic nature of the film. The resistance of the film was 840 Ω.
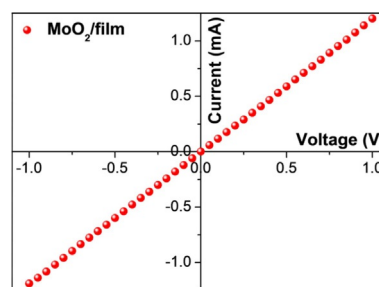
Figure 7. I-V characteristics of MoO$_2$ NSs film.

Electrochemical studies of MoO$_2$ film and powder

The electrocatalytic activities of the as-synthesized MoO$_2$/FTO films as well as the powder were investigated by linear sweep voltammetry (LSV) measurements in 0.5 M H$_2$SO$_4$. The number of active sites and conductivity are major factors that determine the HER performance of the catalyst. Hydrogen annealing has proven to be an effective strategy to expose more active sites.[14] Hence, MoO$_2$ powder and MoO$_2$ film/FTO were annealed under hydrogen at 400 °C for 1 hour to improve activity towards HER. The samples (H-MoO$_2$ powder and H-MoO$_2$ film/FTO) were characterized to determine any morphological and structural changes after hydrogen annealing. FESEM analysis (Figure 8) shows that there is a change in the morphology. The discs are seen to fuse and grow bigger with a change in the orientation of the crystallites. In the case of MoO$_2$/FTO, many of the edge facets are exposed after annealing. The crystal structure and chemical nature of the hydrogen-annealed samples remain unaltered as supported by XRD and Raman spectroscopic analysis (Figure S18).

However, a change in the preferred orientation of MoO$_2$ film on FTO from (200) to (110) is noticeable from the XRD pattern, in accordance with the change in crystallite orientation in the FESEM analysis. The intensity of the (110) plane has also increased in the hydrogen-annealed MoO$_2$ powder. XPS analysis indicates that there are slight changes in the surface oxygen species due to hydrogen annealing (Figure S19). The obtained Mo 3d spectra (Figure S19b) is almost similar to that of the un-
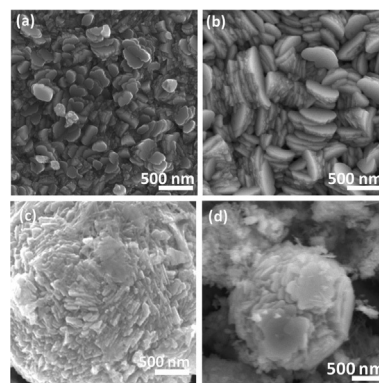
Figure 8. FESEM images showing the effect of hydrogen annealing on MoO$_2$ NSs (a,b) film on FTO and (c,d) powder from solution (a,c) before and (b,d) after annealing.

annealed MoO_2, in which peaks due to Mo^{4+} appear at 229.4 and 232.6 eV corresponding to Mo $3d_{5/2}$ and Mo $3d_{3/2}$ and diminished peaks from Mo^{5+} situated at 231.1 and 235.4 eV, respectively. O 1s spectra (Figure S19c) of $H-MoO_2$ shows that there is a slight decrease in the surface-adsorbed oxygen (530.7 eV) and accordingly an increase in -OH species (532.1 eV) after annealing under hydrogen.

Figure 9a,b shows the LSV curves and Tafel plots of the as-synthesized MoO_2 NSs. The LSV curves and the Tafel plots of MoO_2 NSs were compared with that of the benchmark catalyst Pt/C (20 wt.%). $H-MoO_2$ powder and $H-MoO_2$ film/FTO have lower onset potentials and higher current densities than those
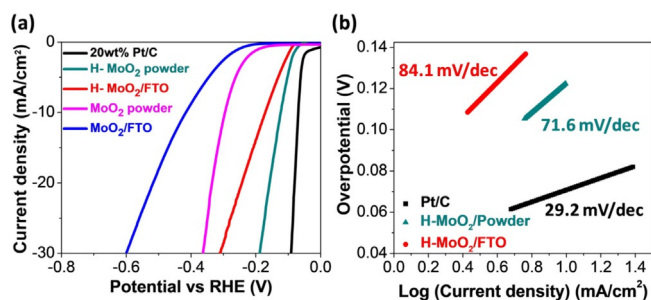

Figure 9. (a) LSV curves and (b) Tafel plots of MoO_2 film/FTO and MoO_2 powder in 0.5 M H_2SO_4 aqueous solution.

of the as-synthesized MoO_2. $H-MoO_2$ powder exhibits the highest HER activity with an onset potential of about 46 mV. To obtain cathodic current densities of 10 and 20 mA cm^{-2}, overpotentials of about 123 and 158 mV are required, respectively. In the case of $H-MoO_2$ film/FTO, an onset potential of 72 mV was observed, and also overpotentials of 171 and 243 mV were needed to achieve cathodic current densities of 10 and 20 mA cm^{-2}, respectively. The Tafel slope of 71.6 mV dec^{-1} was obtained for $H-MoO_2$ powder, whereas a slope of 84.1 mV dec^{-1} was obtained for $H-MoO_2$ film/FTO. Commercial 20 wt.% Pt/C catalysts showed a Tafel slope of 29.2 mV dec^{-1}. The electrocatalytic activity of MoO_2 NSs is in the order of $H-MoO_2$ powder > $H-MoO_2$/FTO > MoO_2 powder > MoO_2/FTO.

The Tafel slope obtained for MoO_2 NSs indicates that HER proceeds by a Volmer–Heyrovsky mechanism, whereas the benchmark catalyst Pt/C follows a Volmer–Tafel mechanism.[37] By using the extrapolation method on the Tafel plots, the exchange current densities were calculated as 0.36 mA cm^{-2} for $H-MoO_2$ powder and 0.16 mA cm^{-2} for $H-MoO_2$ film/FTO. The stability of both samples was tested by applying a constant potential for 12 hours at 10 mA cm^{-2} cathodic current density (current vs time, i–t curve in Figure S20a,b) and performing LSV for 2000 cycles (Figure S20c,d). It can be clearly seen that $H-MoO_2$ powder and $H-MoO_2$ film/FTO have superior stability towards long-term HER. $H-MoO_2$/FTO showed excellent stability even after 12 hours of testing. Figure S21 shows the Raman spectroscopic and XRD analysis of samples before and after HER. It is evident that MoO_2 did not undergo any chemical modification after HER measurements. A comparison with literature data demonstrates that the synthesized MoO_2 powder in

this work is one among the best reported Mo-based electrocatalysts (Table S6), emphasizing its promising application as a HER catalyst. The hydrogen gas (a confirmation test for the evolved hydrogen gas was carried out by a squeaky pop test) evolved in the case of $H-MoO_2$/FTO was collected by water displacement method in an inverted graduated tube over the electrode.[38a] The faradaic yield was estimated to be $\approx 80\%$ from the ratio of the amount of hydrogen collected for 12 hours when subjected to potentiostatic electrolysis in 0.5 M H_2SO_4 at 10 mA cm^{-2} cathodic current density to the calculated theoretical value assuming all electrons passing through the circuit participate in the reduction reaction.

Electrochemical impedance spectroscopy (EIS) measurements were carried out to study the kinetics of various MoO_2-modified electrodes towards HER in the frequency range of 10^6 to 0.1 Hz. Figure 10 shows the Nyquist plots of MoO_2/FTO and
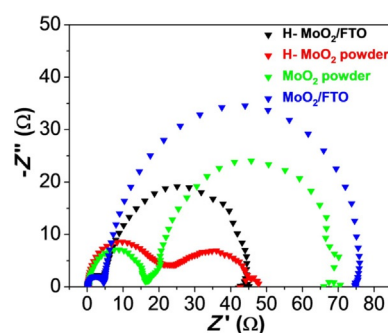

Figure 10. Electrochemical impedance spectra of MoO_2 NSs on FTO and GCE before and after hydrogen annealing.

MoO_2 powder at 250 mV. The first semicircle in the higher frequency region is related to bulk resistance arising from the substrate/catalyst interface and internal resistance of the electrocatalyst. The lower resistance value for MoO_2/FTO compared to that of the MoO_2 powder/glassy carbon electrode (GCE) is attributed to the preparation of the film sample on FTO achieved by in situ chemical growth, which causes effective electron transport yielding low substrate/electrocatalyst resistance corresponding to non-faradaic processes. The lower-frequency semicircle corresponds to charge-transfer resistance (R_{ct}) between electrocatalyst/electrolyte interfaces associated with HER kinetics.[38] The faradaic nature of R_{ct} is confirmed by the potential-dependent nature as shown in the impedance measurements carried out at different HER potential regions (Figure S22). Thus, $H-MoO_2$ powder with the lowest R_{ct} among the various samples shows the highest HER activity. The electrochemical surface area determined from the double-layer capacitance measurement (Figure S23) is higher for the $H-MoO_2$ powder, leading to faster reaction kinetics.[39]

We have tried to understand the drastic improvement in the HER activity after hydrogen annealing. It has been reported that during hydrogen annealing of MoO_3, hydrogen intercalates into the layers to form H_xMoO_3, which slowly decomposes into MoO_2.[14,23a] Hydrogen annealing of WO_3 has been shown to form $WO_{2.9}$, which is highly active for HER. In this case, hy-

drogen treatment caused local atomic structure modulation, creating active W sites energetically favorable for the adsorption of H.[40] In our study, the superior HER activity and stability of H-MoO$_2$ could be due to a combined effect of various factors. Foremost, we have observed from XRD analysis that the preferred crystallite orientation of MoO$_2$ changes to (110) after hydrogen annealing (Figure 2 and Figure S18). A significant improvement in the (110) intensity ($\approx$30% to $\approx$60% in the case of the film) is observed, and accordingly, electrochemical activity is doubled. The overpotentials required for 10 and 20 mA cm^{-2} cathodic current densities are nearly halved after hydrogen annealing. The crystal facets can have direct influence on HER activity because of the energetics involved in H adsorption. This has been well-studied in the case of Pt, of which (110) planes are shown to be more active.[41] In the case of Co$_3$O$_4$, the abundance of Co^{3+} on (110) planes are shown to be responsible for high oxygen evolution reaction (OER) and HER.[42] In the present case, the exposure of (110) facets of MoO$_2$ might also result in the generation of energetically favorable active sites for HER. Further, the morphology of the sample indicates flashing of fringe facets or edge states after hydrogen annealing. In addition, as seen from the XPS spectra and impedance analysis, MoO$_2$ offers less charge-transfer resistance after hydrogen annealing, and this may be a result of the removal of lattice-incorporated water and the reduction of surface oxide species. Experiments are now in progress to obtain direct evidence for HER activity dependent on the morphology and crystal plane.

Conclusion

MoO$_2$ NSs with monoclinic crystal structure were successfully synthesized both in solution and on a rigid substrate (FTO) through a hydrothermal process involving CA as the surfactant. The film on FTO consisted of disc-shaped nanostructures, whereas the powder form contained microspheres formed by disc-shaped NSs. Interestingly, both FTO and solution-phase MoO$_2$ NSs were devoid of any other polymorphic forms. A systematic growth study performed by varying the synthesis conditions indicated that a slight variation in temperature and pH led to the formation of different polymorphs and diverse morphology of MoO$_2$ NSs ranging from disc, flower and hexagonal shapes to square rods and so on. The metallic nature of the film was revealed from I-V measurements. IR and NMR spectroscopic studies revealed the role of CA as a reducing agent and as a structure-directing agent. A time-dependent study showed faster reaction kinetics for MoO$_2$ formation on FTO than that in solution. The electrochemical studies revealed that MoO$_2$ NSs are excellent candidates for hydrogen evolution reaction catalysts. HER catalytic activity including the onset potential, current density and Tafel slope of MoO$_2$ NSs are effectively improved by hydrogen annealing, and this can be attributed to the combined effect of factors such as an increase in active sites, exposure of (110) facets, reduction of surface oxides and less charge-transfer resistance at the MoO$_2$/electrolyte interface.

Experimental Section

Materials

AHM (EMPARTA), CA (C$_6$H$_8$O$_7$, anhydrous, 99.5%), concentrated nitric acid (69%) and HF (48% GR) were purchased from Merck. AA and MoAcac were purchased from Sigma-Aldrich, and MoCl$_5$ (99.8%) was purchased from Alfa Aesar. All other reagents were of analytical grade and used without further purification. All aqueous solutions were prepared with Milli-Q water. An aqueous solution of 0.5 M H$_2$SO$_4$ (Sigma–Aldrich, 99.95%) was prepared from deionized water for use as electrolyte in the electrochemical measurements.

Synthesis of MoO$_2$ films and powder

MoO$_2$ NSs were grown by hydrothermal synthesis on FTO glass substrates (1$\times$1 cm), which were ultrasonically cleaned for 15 min prior to the synthesis with trichloroethylene, acetone and methanol, and then further dried under a nitrogen stream and on a hot plate at 80°C. In the standard reaction defined above, FTO substrates were placed in a slanted fashion with the conducting side facing downwards into an autoclave containing thoroughly mixed solutions of 0.02 M AHM and 0.1 M CA in Milli-Q water (40 mL). The autoclave was then maintained at 200°C for 12 h. After the synthesis, the substrates were thoroughly washed with deionized water and ethanol several times and dried under nitrogen flow. The solution obtained after the reaction was also centrifuged to collect the black precipitate which was washed and dried (Figure 1b).

The synthesis was also performed by varying several parameters such as the concentration of the surfactant (0.1, 0.2 and 0.4 M CA), Mo precursor type (AHM, MoCl$_5$ and MoAcac), substrates (FTO, glass, SiO$_2$/Si and Si), concentration of acid (volume of 1 M HNO$_3$), temperature (120, 150 and 200°C), time (12, 30 and 48 h) and surfactant type (CA and AA). The effect of annealing under nitrogen and air on the morphology and crystal structure of MoO$_2$ NSs was also investigated.

Characterization

A FESEM system (TESCAN MIRA3 LM, Brno, Czech Republic) with an attached Bruker Nano XFlash 6│30 was used to study surface morphology and perform EDS. XRD analyses were carried out with a Rigaku SmartLab diffractometer with Cu$_{K\alpha}$ (40 kV, 30 mA), and Raman spectroscopic studies were carried out with a HORIBA XploRA PLUS spectrometer. A Tecnai (G2 F30, S-TWIN TEM, 300 kV) TEM system was used to perform the structural characterization. XPS measurements were carried out with an AXIS Ultra spectrometer (Kratos) integrated with magnetic immersion lens, charge neutralization system and spherical mirror analyser. The thermal stability of the precursors was examined by means of TGA and DTA (NETZSCH, STA 2500) at a heating rate of 5°C min^{-1} from 25 to 600°C. IR spectra were recorded using KBr pellets with a FTIR spectrometer (PerkinElmer, Spectrum 1000) in the range of 400–4000 cm^{-1}. Solid-state ^{13}C NMR spectroscopic analyses were carried out with a JEOL (400 MHz) high-resolution multinuclear FT-NMR spectrometer.

Electrochemical measurements

All electrochemical experiments were conducted with a potentiostat (CH Instruments, CHI 660E), with a three-electrode configuration consisting of Pt wire as the counter electrode and saturated Hg/Hg$_2$SO$_4$ as the reference electrode in 0.5 M H$_2$SO$_4$ (pH $\approx$1) electrolyte. A GCE (0.07 cm^2 geometric surface area) was used as the

working electrode to study HER activity of the powder samples. All voltammetric measurements were obtained at a scan rate of $5\,\text{mV s}^{-1}$. Nafion (1 wt.% in 1:3 isopropyl alcohol/water) was used as a binder for GCE measurement.

Acknowledgements

Conflict of interest

The authors declare no conflict of interest.

[1] Y. Qiu, S.-F. Leung, Q. Zhang, B. Hua, Q. Lin, Z. Wei, K.-H. Tsui, Y. Zhang, S. Yang, Z. Fan, *Nano Lett.* **2014**, *14*, 2123–2129.

[2] J. D. Benck, T. R. Hellstern, J. Kibsgaard, P. Chakthranont, T. F. Jaramillo, *ACS Catal.* **2014**, *4*, 3957–3971.

[3] a) D. Jariwala, V. K. Sangwan, L. J. Lauhon, T. J. Marks, M. C. Hersam, *ACS Nano* **2014**, *8*, 1102–1120; b) V. Ramakrishnan, H. Kim, J. Park, B. Yang, *RSC Adv.* **2016**, *6*, 9789–9795; c) K. Bramhaiah, N. S. John, *RSC Adv.* **2013**, *3*, 7765–7773; d) K. K. Singh, V. Ramakrishnan, R. Prabhu, N. S. John, *CrystEngComm* **2017**, *19*, 6568–6572.

[4] D. O. Scanlon, G. W. Watson, D. Payne, G. Atkinson, R. Egdell, D. Law, *J. Phys. Chem. C* **2010**, *114*, 4636–4645.

[5] a) Q. Zhang, X. Li, Q. Ma, Q. Zhang, H. Bai, W. Yi, J. Liu, J. Han, G. Xi, *Nat. Commun.* **2017**, *8*, 14903; b) Z. Xiang, Q. Zhang, Z. Zhang, X. Xu, Q. Wang, *Ceram. Int.* **2015**, *41*, 977–981; c) B. Hu, L. Mai, W. Chen, F. Yang, *ACS Nano* **2009**, *3*, 478-482.

[6] J. Morlot, N. Uyttebroeck, D. Agustin, R. Poli, *ChemCatChem* **2013**, *5*, 601–611.

[7] S.-W. Liu, C.-C. Lee, A.-K. Cheng, C.-F. Lin, Y.-Z. Li, T.-H. Su, *Jpn. J. Appl. Phys.* **2015**, *54*, 03CC01.

[8] M. Iwase, M.-o. Yasuda, T. Mori, *Electrochim. Acta* **1979**, *24*, 261–266.

[9] Y. Zhao, Y. Zhang, Z. Yang, Y. Yan, K. Sun, *Sci. Technol. Adv. Mater.* **2013**, *14*, 043501.

[10] H. Du, X. Xie, Q. Zhu, L. Lin, Y.-F. Jiang, Z.-K. Yang, X. Zhou, A.-W. Xu, *Nanoscale* **2015**, *7*, 5752–5759.

[11] Y. Jin, H. Wang, J. Li, X. Yue, Y. Han, P. K. Shen, Y. Cui, *Adv. Mater.* **2016**, *28*, 3785–3790.

[12] R. S. Patil, M. Uplane, P. S. Patil, *Int. J. Electrochem. Sci.* **2008**, *3*, 259–265.

[13] Y. Liang, Z. Yi, S. Yang, L. Zhou, J. Sun, Y. Zhou, *Solid State Ionics* **2006**, *177*, 501–505.

[14] Y. Jin, P. K. Shen, *J. Mater. Chem. A* **2015**, *3*, 20080–20085.

[15] S. Ashraf, C. S. Blackman, G. Hyett, I. P. Parkin, *J. Mater. Chem.* **2006**, *16*, 3575–3582.

[16] D. Wang, D. S. Su, R. Schlögl, *Z. Anorg. Allg. Chem.* **2004**, *630*, 1007–1014.

[17] M. Camacho-López, L. Escobar-Alarcón, E. Haro-Poniatowski, *Appl. Phys. A* **2004**, *78*, 59–65.

[18] B. Guo, X. Fang, B. Li, Y. Shi, C. Ouyang, Y.-S. Hu, Z. Wang, G. D. Stucky, L. Chen, *Chem. Mater.* **2012**, *24*, 457–463.

[19] B. Zhang, Y. Xue, A. Jiang, Z. Xue, Z. Li, J. Hao, *ACS Appl. Mater. Interfaces* **2017**, *9*, 7217–7223.

[20] I. Roger, R. Moca, H. N. Miras, K. G. Crawford, D. A. Moran, A. Y. Ganin, M. D. Symes, *J. Mater. Chem. A* **2017**, *5*, 1472–1480.

[21] E. Zhou, C. Wang, Q. Zhao, Z. Li, M. Shao, X. Deng, X. Liu, X. Xu, *Ceram. Int.* **2016**, *42*, 2198–2203.

[22] A. Bhaskar, M. Deepa, T. Rao, U. Varadaraju, *J. Power Sources* **2012**, *216*, 169–178.

[23] a) A. Borgschulte, O. Sambalova, R. Delmelle, S. Jenatsch, R. Hany, F. Nüesch, *Sci. Rep.* **2017**, *7*, 40761; b) P. A. Spevack, N. McIntyre, *J. Phys. Chem.* **1993**, *97*, 11020–11030.

[24] B. Li, Y. Liang, X. Yang, Z. Cui, S. Qiao, S. Zhu, Z. Li, K. Yin, *Nanoscale* **2015**, *7*, 16704–16714.

[25] a) A. Bee, R. Massart, S. Neveu, *J. Magn. Magn. Mater.* **1995**, *149*, 6–9; b) A. P. LaGrow, B. Ingham, M. F. Toney, R. D. Tilley, *J. Phys. Chem. C* **2013**, *117*, 16709–16718.

[26] Z. Y. Banyamin, P. J. Kelly, G. West, J. Boardman, *Coatings* **2014**, *4*, 732–746.

[27] a) A. Chithambararaj, N. R. Yogamalar, A. C. Bose, *Cryst. Growth Des.* **2016**, *16*, 1984–1995; b) A. Chithambararaj, A. C. Bose, *CrystEngComm* **2014**, *16*, 6175–6186.

[28] M. U. Rothmann, W. Li, Y. Zhu, U. Bach, L. Spiccia, J. Etheridge, Y.-B. Cheng, *Nat. Commun.* **2017**, *8*, 14547.

[29] a) H. Hofmeister, *Z. Kristallogr. Cryst. Mater.* **2009**, *224*, 528–538; b) F. Lee, G. Parkinson, M. Reyhani, W. Van Bronswijk, C. Vernon, *Sci. Access* **2004**, *2*, 230–231; c) C. Sweegers, W. Van Enckevort, H. Meekes, P. Bennema, I. Hiralal, A. Rijkeboer, *J. Cryst. Growth* **1999**, *197*, 244–253; d) H. Wang, T. B. Shrestha, M. T. Basel, M. Pyle, Y. Toledo, A. Konecny, P. Thapa, M. Ikenberry, K. L. Hohn, V. Chikan, *J. Mater. Chem. B* **2015**, *3*, 4647–4653.

[30] a) L. Sacconi, R. Cini, *J. Chem. Phys.* **1950**, *18*, 1124; b) W. Treadwell, Y. Schaeppi, *Helv. Chim. Acta* **1946**, *29*, 771–783.

[31] A. Goodarzi, Y. Sahoo, M. Swihart, P. Prasad, *MRS Online Proc. Libr. Archive* **2003**, 789.

[32] a) J. Kubicki, L. Schroeter, M. Itoh, B. Nguyen, S. Apitz, *Geochim. Cosmochim. Acta* **1999**, *63*, 2709–2725; b) I. A. Mudunkotuwa, V. H. Grassian, *J. Am. Chem. Soc.* **2010**, *132*, 14986–14994.

[33] a) S. Mallakpour, F. Sirous, *Polym.-Plast. Technol. Eng.* **2015**, *54*, 532–540; b) D. S. Todorovsky, D. G. Dumanova, R. V. Todorovska, M. M. Getsova, *Croat. Chem. Acta* **2002**, *75*, 155–164.

[34] Z. Yang, Q.-H. Liu, L. Yang, *Mater. Res. Bull.* **2007**, *42*, 221–227.

[35] B. Ren, M. Fan, Q. Liu, J. Wang, D. Song, X. Bai, *Electrochim. Acta* **2013**, *92*, 197–204.

[36] a) E. Aivazoglou, E. Metaxa, E. Hristoforou, *AIP Adv.* **2018**, *8*, 048201; b) D. Chen, L. Gao, *J. Colloid Interface Sci.* **2004**, *279*, 137–142; c) M. Li, K. K. Wong, S. Mann, *Chem. Mater.* **1999**, *11*, 23–26; d) T.-M. Liu, J. Yu, C. A. Chang, A. Chiou, H. K. Chiang, Y.-C. Chuang, C.-H. Wu, C.-H. Hsu, P.-A. Chen, C.-C. Huang, *Sci. Rep.* **2014**, *4*, 5593.

[37] a) S. A. Vilekar, I. Fishtik, R. Datta, *J. Electrochem. Soc.* **2010**, *157*, B1040–B1050; b) X. Xie, L. Lin, R.-Y. Liu, Y.-F. Jiang, Q. Zhu, A.-W. Xu, *J. Mater. Chem. A* **2015**, *3*, 8055–8061.

[38] a) C. Iv, Z. Huang, Q. Yang, C. Zhang, *Energy Technol.* **2018**, *6*, 1–9; b) J. Guo, J. Wang, Z. Wu, W. Lei, J. Zhu, K. Xia, D. Wang, *J. Mater. Chem. A* **2017**, *5*, 4879–4885; c) X. Chen, G. Liu, W. Zheng, W. Feng, W. Cao, W. Hu, P. Hu, *Adv. Funct. Mater.* **2016**, *26*, 8537–8544.

[39] J. Jia, W. Zhou, Z. Wei, T. Xiong, G. Li, L. Zhao, X. Zhang, H. Liu, J. Zhou, S. Chen, *Nano Energy* **2017**, *41*, 749–757.

[40] Y. H. Li, P. F. Liu, L. F. Pan, H. F. Wang, Z. Z. Yang, L. R. Zheng, P. Hu, H. J. Zhao, L. Gu, H. G. Yang, *Nat. Commun.* **2015**, *6*, 8064.

[41] N. Marković, B. Grgur, P. N. Ross, *J. Phys. Chem. B* **1997**, *101*, 5405–5413.

[42] Q. Liu, Z. Chen, Z. Yan, Y. Wang, E. Wang, S. Wang, S. Wang, G. Sun, *ChemElectroChem* **2018**, *5*, 1080–1086.